Title

Phonon Polaritons in Monolayers of Hexagonal Boron Nitride.

Journal

Advanced materials (Deerfield Beach, Fla.), 31(37)

ISSN

0935-9648

Authors

Dai, Siyuan
Fang, Wenjing
Rivera, Nicholas
et al.

Publication Date

2019-09-01

DOI

10.1002/adma.201806603

Peer reviewed

ADVANCED MATERIALS
www.advmat.de

Phonon Polaritons in Monolayers of Hexagonal Boron Nitride

Siyuan Dai, Wenjing Fang, Nicholas Rivera, Yijing Stehle, Bor-Yuan Jiang, Jialiang Shen, Roland Yingjie Tay, Christopher J. Ciccarino, Qiong Ma, Daniel Rodan-Legrain, Pablo Jarillo-Herrero, Edwin Hang Tong Teo, Michael M. Fogler, Prineha Narang, Jing Kong, and Dimitri N. Basov**

Phonon polaritons in van der Waals materials reveal significant confinement accompanied with long propagation length: important virtues for tasks pertaining to the control of light and energy flow at the nanoscale. While previous studies of phonon polaritons have relied on relatively thick samples, here reported is the first observation of surface phonon polaritons in single atomic layers and bilayers of hexagonal boron nitride (hBN). Using antenna-based near-field microscopy, propagating surface phonon polaritons in mono- and bilayer hBN microcrystals are imaged. Phonon polaritons in monolayer hBN are confined in a volume about one million times smaller than the free-space photons. Both the polariton dispersion and their wavelength–thickness scaling law are altered compared to those of hBN bulk counterparts. These changes are attributed to phonon hardening in monolayer-thick crystals. The data reported here have bearing on applications of polaritons in metasurfaces and ultrathin optical elements.

Phonon polaritons are collective modes formed by hybridization of free-space photons with lattice vibrations in polar insulators. These modes exhibit a high density of states, a strong confinement of the electric field,[1,2] and a relatively low loss comparable to that of state-of-the-art plasmonic structures.[3,4] These virtues make the polaritons promising candidates for superlensing,[5] super-Planckian heat transfer,[6] wavefront control,[7,8] and other novel applications. Besides hexagonal boron nitride (hBN),[9–15] phonon polaritons have been investigated in SiC,[5,16] GaAs,[17,18] $LiTaO_3$,[19] MoO_3,[20,21] as well as in metamaterials.[8,22] In these systems, phonon polaritons span a broad range of frequencies, from terahertz to mid-infrared (mid-IR).

An intriguing aspect of hBN in the context of phonon polariton physics and applications is its optical hyperbolicity,[9,10,23] i.e., the existence of a frequency band between transverse optical (TO) mode at ω_{TO} and longitudinal optical (LO) mode at ω_{LO}: $\omega_{TO} < \omega < \omega_{LO}$. In this latter frequency region, the basal-plane permittivity of hBN Re $\varepsilon^t < 0$ whereas the z-axis permittivity is positive Re $\varepsilon^z > 0$. Theory predicts[14] that the polariton dispersion within the hyperbolic frequency region consists of multiple branches whose number is equal to the number N of atomic layers. In experiment, only the so-called principal branch is typically observed, as is the case here. The theory further predicts that the

Prof. S. Dai, J. Shen
Materials Research and Education Center
Department of Mechanical Engineering
Auburn University
Auburn, AL 36849, USA
E-mail: sdai@auburn.edu
Dr. W. Fang, Prof. J. Kong
Department of Electrical Engineering & Computer Sciences
Massachusetts Institute of Technology
Cambridge, MA 02139, USA
N. Rivera, C. J. Ciccarino, Prof. P. Narang
John A. Paulson School of Engineering and Applied Sciences
Harvard University
Cambridge, MA 02139, USA
N. Rivera, Dr. Q. Ma, D. Rodan-Legrain, Prof. P. Jarillo-Herrero
Department of Physics
Massachusetts Institute of Technology
Cambridge, MA 02139, USA
The ORCID identification number(s) for the author(s) of this article can be found under https://doi.org/10.1002/adma.201806603.
Prof. Y. Stehle
Sichuan University Pittsburgh Institute
Sichuan University
Sichuan, Chengdu 610017, China
Dr. B.-Y. Jiang, Prof. M. M. Fogler
Department of Physics
University of California, San Diego
La Jolla, CA 92093, USA
R. Y. Tay, Prof. E. H. T. Teo
School of Electrical and Electronic Engineering
Nanyang Technology University
50 Nanyang Avenue, Singapore 639798, Singapore
Prof. D. N. Basov
Department of Physics
Columbia University
New York, NY 10027, USA
E-mail: db3056@columbia.edu

DOI: 10.1002/adma.201806603

dispersion of this branch near the in-plane TO frequency ω_{TO} = 1367 cm^{-1} is linear in polariton momentum k

$$\omega = \omega_{TO} + Nv_1k, \quad k_0 << k << 1/(Nd_1) \tag{1}$$

Here, k_0 is the momentum of the IR photon, $\lambda_0 = 2\pi/k_0$ is the corresponding wavelength, d_1 = 0.34 nm is the hBN interlayer distance, and v_1 is a characteristic velocity discussed below. Equation (1) implies that the polariton dispersion can be tuned by varying N, which has been verified by imaging of phonon polariton propagation in real space.[9] (Tuning of the polariton dispersion by electrostatic gating[22] and temperature[24,25] has also been demonstrated.) Because of weak van der Waals (vdW) coupling of the layers, N can be controlled with atomic precision using exfoliation or chemical-vapor-deposition techniques. However, imaging of phonon polaritons has so far been achieved only in multilayer (bulk) hBN crystals.[8,9] In the present work, we report imaging of phonon polaritons in monolayer and bilayer hBN. Our principal finding is that polariton modes harden (shift to higher frequency) in hBN monolayers: the ultimate limit of a single atomic plane. A possible reason for the phonon hardening may be a small decrease of the in-plane lattice constant compared to the bulk value due to the lack of interlayer interaction.[26,27] Theoretical calculations of this effect have not yet reached a consensus, predicting either softening[15] or hardening[26] of the phonon mode. Therefore, our experimental results provide an empirical reference point for the lattice dynamics models of atomically thin vdW layers. Our results may also be relevant for the development of ultrathin phononic elements for mid-IR optics.[28] Note that in monolayers, the notion of the z-axis permittivity and therefore hyperbolic collective modes[10,11,13,14] is not applicable. The phonon polaritons we have imaged are better understood as surface modes. Their field distribution decays exponentially away from hBN. Nevertheless, Equation (1) remains valid even for N = 1 as we will discuss below and also in the Supporting Information (Sections S2 and S3).

Our monolayer and bilayer hBN samples were grown[29] by low-pressure chemical vapor deposition (LP-CVD) method on iron foils and then transferred to the SiO_2/Si substrates (see the Experimental Section for details). We performed the IR nanoimaging of these samples using the scattering-type scanning near-field optical microscopy (s-SNOM).[16] The s-SNOM, based on a tapping-mode atomic force microscope (AFM), simultaneously yields the topography and nano-IR images over the scanned area. In the experiment, a continuous-wave IR laser (solid arrow) is focused on the apex of a metalized AFM tip, which acts as an optical antenna generating a strong near field (**Figure 1**a). This field launches phonon polaritons in hBN[30] that propagate to the edge of the sample and get reflected back to the tip. The modified near field under the tip creates scattered IR light, which is detected in the far field. The experimental observables are the near-field amplitude $S(\omega)$ and phase $\Phi(\omega)$ detected in the backscattering geometry and demodulated at the third harmonics of the tip tapping frequency. The demodulation eliminates far-field background and isolates the genuine near-field signal.[31]

Our representative s-SNOM images are shown in Figure 1b–d. The hBN crystals have triangular shapes[32] and exhibit an evident s-SNOM phase $\Phi(\omega)$ contrast that can be clearly distinguished from that of the SiO_2 substrate. Close to sample edges, we find oscillations or fringes characteristic of polaritonic standing waves in 2D materials.[1,2] These fringes are aligned parallel to the hBN edges in both monolayer and bilayer crystals. Line traces (taken along the blue and red dotted lines in Figure 1b) demonstrate polariton fringes as peaks and valleys in **Figure 2**a,b. The fringes are observed only at frequencies above the in-plane TO frequency of bulk hBN, ω_{TO} = 1367 cm^{-1}. Our imaging data reveal a systematic evolution of the fringes with ω (Figure 1b–d): as ω increases, the fringes move closer to the hBN edge (L = 0, see also line profiles in Figure 2a,b), indicating a decreasing period of the fringes. Such hallmarks of dispersive phenomena validate the assignment of the fringes to surface phonon polaritons[33] in hBN. The fringes form along the hBN edges due to the interference of the tip-launched and edge-reflected surface phonon polaritons.[9,11,13,34] Note that the phase images are better suited for visualizing phonon polaritons in ultrathin samples (Figure 1) because the fringes in $\Phi(\omega)$ are closer to the crystal edges[11,35] compared with those in $S(\omega)$ and so suffer less damping. Nevertheless, we utilized both $\Phi(\omega)$ and $S(\omega)$ for the quantitative analysis (see Section S1 of Supporting

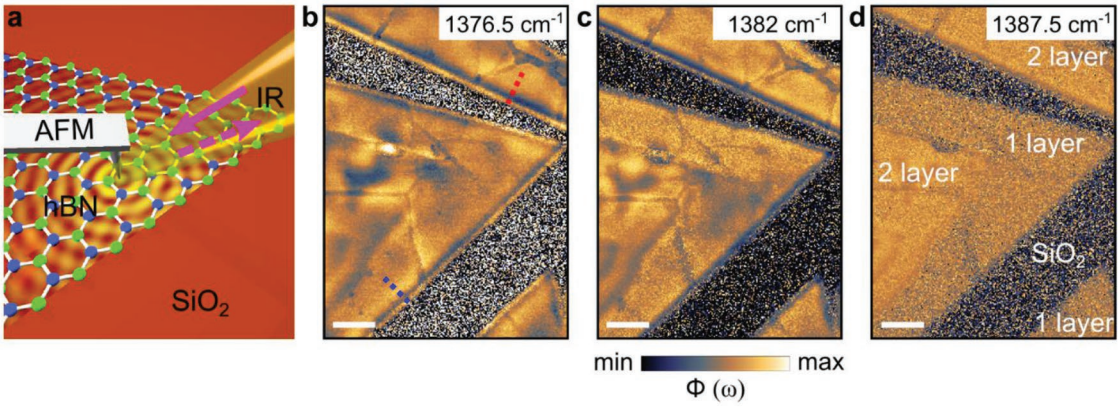

Figure 1. Nanoimaging of surface phonon polaritons in monolayer and bilayer hBN. a) Experiment setup. The AFM tip and hBN sample are illuminated by the IR beam (solid magenta arrow) from a QCL. Propagating surface phonon polariton waves are launched and detected by the AFM tip (dotted magenta arrow). b–d) s-SNOM phase images of surface phonon polaritons in monolayer and bilayer hBN at IR frequency ω = 1376.5, 1382, and 1387.5 cm^{-1}. Scale bar: 500 nm.

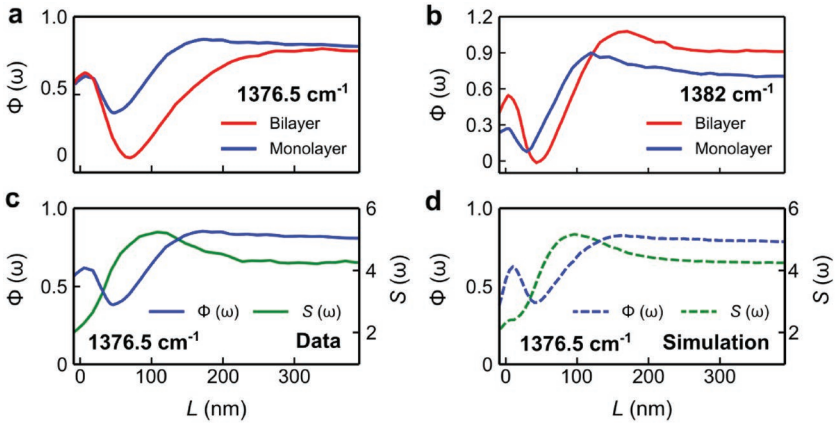

Figure 2. Line traces of the surface phonon polaritons in monolayer and bilayer hBN. Line traces of s-SNOM phase $\Phi(\omega)$ taken along the dotted cuts in Figure 1 at IR frequency a) $\omega = 1376.5$ cm^{-1} and b) 1382 cm^{-1}. c) Line traces of s-SNOM phase $\Phi(\omega)$ and amplitude $S(\omega)$ at $\omega = 1376.5$ cm^{-1}. d) Simulation of s-SNOM phase $\Phi(\omega)$ and amplitude $S(\omega)$ at $\omega = 1376.5$ cm^{-1}.

Information). For each frequency ω, we extracted the polariton wavelength λ and the dimensionless damping factor γ by fitting the s-SNOM line profiles of $\Phi(\omega)$ and $S(\omega)$ (Figure 2a,b) to numerically calculated line ones (Supporting Information, Section S1). We also extracted λ by another, simpler method, based on evaluating the peak-to-valley distance in the $\Phi(\omega)$ line traces. The two methods gave consistent results. The inferred dispersion of the phonon polaritons is displayed in **Figure 3** where we plot frequency ω versus the confinement factor $\lambda_0/\lambda = k/k_0$. Figure 3a shows the results for a bilayer (triangles) and Figure 3b for a monolayer (dots). In both cases, the confinement factor λ_0/λ can approach or exceed 60 (Figure 3). Accordingly, the mode volume λ^3/π[22] of polaritons is reduced compared to the mode volume $(\lambda_0)^3$ of free-space photons[36] by a factor up to 10^6.

We now compare the experimental dispersions with Equation (1). There are several complementary theoretical approaches to deriving the characteristic velocity v_1 in Equation (1) (see the Supporting Information, Section S2); among these, continuum electrodynamics is the simplest approach. This approach predicts that v_1 is determined by the in-plane permittivity ε^t of hBN and the permittivity ε_2 of SiO_2 substrate. The z-axis permittivity of hBN gives only subleading corrections because of the strong inequality $|\varepsilon^t| >> \varepsilon^z$ near ω_{TO}. This explains why continuum electrodynamics is valid not only for relatively thick[9,23,34] but also for atomically thin hBN crystals. The red dash-dotted line in Figure 3a corresponding to permittivity ($\omega_{TO} = 1367$ cm^{-1} , $\omega_{LO} = 1614$ cm^{-1}, etc.)[4,10] is in a quantitative agreement with our data for bilayer hBN (triangles). On the other hand, the blue dashed line in Figure 3b corresponding to the same ω_{TO} and v_1 systematically underestimates the polariton frequency measured in a monolayer (dots). In addition, the linear thickness-dependence law for phonon polaritons in bulk hBN[9,23,34] fails in the case of monolayer and bilayer samples. Provided ω_{TO} and v_1 were the same in the monolayer and the bilayer, the ratio of their polariton wavelengths at a given frequency would be equal to 2 (blue dashed line). Instead, the ratio is frequency-dependent and varies from 1.1 to 1.7 (**Figure 4**, black squares). We can account for both discrepancies by assuming that the TO frequency of the monolayer is blueshifted by 3.5 cm^{-1}, giving the dispersion indicated by the green dashed line in Figure 4. Previously, similar mode hardening has been observed in Raman spectroscopy of monolayer hBN[27] and BN nanotubes.[26]

As mentioned above, one possible explanation for the blueshift of phonon resonances in ultrathin hBN is a slight shortening of the B—N bonds[26] due to the lack of interlayer interaction. To further verify this hypothesis we have performed density functional theory calculations[37] taking into account exchange-correlation functionals and vdW interaction. Our calculations reveal a 2 cm^{-1} blueshift of the phonon in monolayer compared with that in bilayer hBN (Supporting Information, Section S2). We note that the phonon mode hardening due to the lack of interlayer interactions is likely to be generic to monolayers of vdW materials, including black phosphorus, transition metal dichalcogenides,[38] nanotubes,[12] and in-plane heterostructures.[39,40]

Because of the signal-to-noise limitations of state-of-the-art nano-IR methods that we utilized in our work, our imaging of surface phonon polaritons in monolayer was restricted to the vicinity of the TO phonon frequency where the dielectric loss in hBN is strong (polariton damping factor $\gamma \sim 0.6$). With an improved spatial resolution, it may become possible to image polaritons at higher frequencies where the dielectric

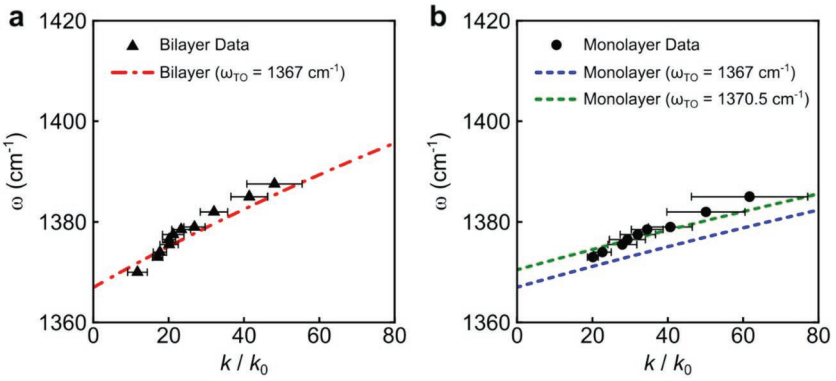

Figure 3. Dispersion of surface phonon polaritons in monolayer and bilayer hBN. a) Frequency (ω)–momentum (k/k_0) dispersion of surface phonon polaritons in bilayer hBN. b) Frequency (ω)–momentum (k/k_0) dispersion of surface phonon polaritons in monolayer hBN. Experimental data (dots for monolayer and triangles for bilayer) are extracted from s-SNOM images in Figure 1. Theoretical results are indicated with blue ($\omega_{TO} = 1367$ cm^{-1}) and green ($\omega_{TO} = 1370.5$ cm^{-1}) dashed curves for monolayer hBN and red ($\omega_{TO} = 1367$ cm^{-1}) dashed-dotted curve for bilayer hBN.

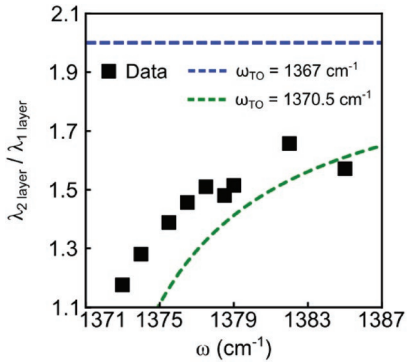

Figure 4. The wavelength ratio between surface phonon polaritons in bilayer (λ_{2layer}) and in monolayer hBN (λ_{1layer}). Experimental data are plotted with black squares. Theoretical results are plotted with the green (monolayer hBN: ω_{TO} = 1370.5 cm^{-1}) and blue (monolayer hBN: ω_{TO} = 1367 cm^{-1}) dashed curve.

loss is smaller.[9] We envision a possibility of tuning phonon polaritons in thin vdW crystals with strain and friction engineering.[41–43] Finally, it may be worth exploring a 1D counterpart of hyperbolic surface polaritons propagating along the hBN edges.[44,45]

Experimental Section

Experimental Setup: The IR nanoimaging of surface phonon polaritons in monolayer and bilayer hBN were performed using an s-SNOM. This s-SNOM, based on a tapping-mode AFM, is a commercial system (www.neaspec.com). In order to launch and detect propagating polaritons, a commercial AFM tip (tip radius ≈10 nm) with a $PtIr_5$ coating was used. In the experiment, the AFM tip was illuminated by monochromatic quantum cascade lasers (QCLs) (www.daylightsolutions.com) covering a frequency range of 900–2300 cm^{-1} in the mid-IR. The phase and amplitude s-SNOM nanoimages were recorded by a pseudo-heterodyne interferometric detection module with an AFM tapping frequency 280 kHz and tapping amplitude around 70 nm. To obtain the background-free signal, the s-SNOM output at the third harmonics of the tapping frequency was demodulated.

Sample Synthesis: Monolayer and bilayer hBN were synthesized using LP-CVD with borazine as the precursor. Before the synthesis of hBN, the Fe foil (Alfa Aesar, 99.99%) was pretreated by annealing it at 1100 °C for 1 h under 10 sccm H_2. During the hBN growth, 0.1 sccm H_2 carrier gas (with borazine vapor) and 100 sccm H_2 at 1100 °C for 1 h were supplied. After the growth, the sample was first cooled with a rate of 5 °C min^{-1} until 700 °C and then to the room temperature without a controlled rate.

To transfer the synthesized hBN, the sample was first coated with a layer of poly(methyl methacrylate) (PMMA, 950 A9, MicroChem, diluted to 4.5% in anisole) at 2500 rpm for 1 min and baked it at 80 °C for 10 min. Before transferring the sample to the SiO2/Si substrate, Fe foil was removed by floating the coated sample on nitric acid (Transene Company Inc.) for 1 h. Finally, the PMMA was washed out by acetone and thermal annealing at 350 °C under 200 sccm H_2 and 200 sccm Ar for 3 h.

Supporting Information

Supporting Information is available from the Wiley Online Library or from the author.

Acknowledgements

This work was supported by the DARPA Driven and Nonequilibrium Quantum Systems (DRINQS) program (agreement D18AC00014). The content of the information does not necessarily reflect the position or the policy of the Government, and no official endorsement should be inferred. Approved for public release; distribution is unlimited. Work on the development of nano-optical methods was supported as part of Programmable Quantum Materials, an Energy Frontier Research Center funded by the U.S. Department of Energy (DOE), Office of Science, Basic Energy Sciences (BES), under award DE-SC0019443. Research on electrodynamics of vdW monolayers is funded by AFOSRFA9550-15-1-0478. D.N.B. is the Gordon and Betty Moore Foundation investigator in quantum materials, EPiQS Initiative Grant GBMF4533. Q.M. and P.J.-H. were supported by the Center for Excitonics, an Energy Frontier Research Center funded by the DOE, Office of Science, BES under award number DESC0001088 and AFOSR Grant FA9550-16-1-0382 as well as the Gordon and Betty Moore Foundation's EPiQS Initiative through Grant GBMF4541 to P.J-H. B.-Y.J. and M.M.F. were supported by ONR-N000014-18-1-2722. W.F. and J.K. acknowledge support from the STC Center for Integrated Quantum Materials, NSFDMR-1231319, and support from U.S. Army Research Office through the MIT Institute for Soldier Nanotechnologies (ISN), under award no. 023674. P.N. is a Moore Inventor Fellow, supported by the Gordon and Betty Moore Foundation. N.R. was supported by Department of Energy Fellowship DE-FG02-97ER25308.

Conflict of Interest

The authors declare no conflict of interest.

Keywords

monolayers, phonon polaritons, van der Waals materials

Received: October 11, 2018
Revised: July 1, 2019
Published online: July 28, 2019

[1] D. N. Basov, M. M. Fogler, F. J. García de Abajo, *Science* **2016**, *354*, aag1992.
[2] T. Low, A. Chaves, J. D. Caldwell, A. Kumar, N. X. Fang, P. Avouris, T. F. Heinz, F. Guinea, L. Martin-Moreno, F. Koppens, *Nat. Mater.* **2016**, *16*, 182.
[3] Z. Fei, A. S. Rodin, G. O. Andreev, W. Bao, A. S. McLeod, M. Wagner, L. M. Zhang, Z. Zhao, M. Thiemens, G. Dominguez, M. M. Fogler, A. H. C. Neto, C. N. Lau, F. Keilmann, D. N. Basov, *Nature* **2012**, *487*, 82.
[4] G. X. Ni, A. S. McLeod, Z. Sun, L. Wang, L. Xiong, K. W. Post, S. S. Sunku, B. Y. Jiang, J. Hone, C. R. Dean, M. M. Fogler, D. N. Basov, *Nature* **2018**, *557*, 530.
[5] T. Taubner, D. Korobkin, Y. Urzhumov, G. Shvets, R. Hillenbrand, *Science* **2006**, *313*, 1595.
[6] S. Shen, A. Narayanaswamy, G. Chen, *Nano Lett.* **2009**, *9*, 2909.
[7] T. Feurer, N. S. Stoyanov, D. W. Ward, J. C. Vaughan, E. R. Statz, K. A. Nelson, *Annu. Rev. Mater. Res.* **2007**, *37*, 317.
[8] P. Li, I. Dolado, F. J. Alfaro-Mozaz, F. Casanova, L. E. Hueso, S. Liu, J. H. Edgar, A. Y. Nikitin, S. Vélez, R. Hillenbrand, *Science* **2018**, *359*, 892.
[9] S. Dai, Z. Fei, Q. Ma, A. S. Rodin, M. Wagner, A. S. McLeod, M. K. Liu, W. Gannett, W. Regan, K. Watanabe, T. Taniguchi,

M. Thiemens, G. Dominguez, A. H. C. Neto, A. Zettl, F. Keilmann, P. Jarillo-Herrero, M. M. Fogler, D. N. Basov, *Science* **2014**, *343*, 1125.
[10] J. D. Caldwell, A. V. Kretinin, Y. Chen, V. Giannini, M. M. Fogler, Y. Francescato, C. T. Ellis, J. G. Tischler, C. R. Woods, A. J. Giles, M. Hong, K. Watanabe, T. Taniguchi, S. A. Maier, K. S. Novoselov, *Nat. Commun.* **2014**, *5*, 5221.
[11] Z. Shi, H. A. Bechtel, S. Berweger, Y. Sun, B. Zeng, C. Jin, H. Chang, M. C. Martin, M. B. Raschke, F. Wang, *ACS Photonics* **2015**, *2*, 790.
[12] X. G. Xu, B. G. Ghamsari, J.-H. Jiang, L. Gilburd, G. O. Andreev, C. Zhi, Y. Bando, D. Golberg, P. Berini, G. C. Walker, *Nat. Commun.* **2014**, *5*, 4782.
[13] E. Yoxall, M. Schnell, A. Y. Nikitin, O. Txoperena, A. Woessner, M. B. Lundeberg, F. Casanova, L. E. Hueso, F. H. L. Koppens, R. Hillenbrand, *Nat. Photonics* **2015**, *9*, 674.
[14] K. H. Michel, B. Verberck, *Phys. Rev. B* **2011**, *83*, 115328.
[15] T. Sohier, M. Gibertini, M. Calandra, F. Mauri, N. Marzari, *Nano Lett.* **2017**, *17*, 3758.
[16] R. Hillenbrand, T. Taubner, F. Keilmann, *Nature* **2002**, *418*, 159.
[17] M. Haraguchi, M. Fukui, S. Muto, *Phys. Rev. B* **1990**, *41*, 1254.
[18] T. Dekorsy, V. A. Yakovlev, W. Seidel, M. Helm, F. Keilmann, *Phys. Rev. Lett.* **2003**, *90*, 055508.
[19] T. Feurer, J. C. Vaughan, K. A. Nelson, *Science* **2003**, *299*, 374.
[20] W. Ma, P. Alonso-González, S. Li, A. Y. Nikitin, J. Yuan, J. Martín-Sánchez, J. Taboada-Gutiérrez, I. Amenabar, P. Li, S. Vélez, C. Tollan, Z. Dai, Y. Zhang, S. Sriram, K. Kalantar-Zadeh, S.-T. Lee, R. Hillenbrand, Q. Bao, *Nature* **2018**, *562*, 557.
[21] Z. Zheng, N. Xu, S. L. Oscurato, M. Tamagnone, F. Sun, Y. Jiang, Y. Ke, J. Chen, W. Huang, W. L. Wilson, A. Ambrosio, S. Deng, H. Chen, *Sci. Adv.* **2019**, *5*, eaav8690.
[22] S. Dai, Q. Ma, M. K. Liu, T. Andersen, Z. Fei, M. D. Goldflam, M. Wagner, K. Watanabe, T. Taniguchi, M. Thiemens, F. Keilmann, G. C. A. M. Janssen, S. E. Zhu, P. Jarillo-Herrero, M. M. Fogler, D. N. Basov, *Nat. Nanotechnol.* **2015**, *10*, 682.
[23] S. Dai, Q. Ma, T. Andersen, A. S. McLeod, Z. Fei, M. K. Liu, M. Wagner, K. Watanabe, T. Taniguchi, M. Thiemens, F. Keilmann, P. Jarillo-Herrero, M. M. Fogler, D. N. Basov, *Nat. Commun.* **2015**, *6*, 6963.
[24] T. G. Folland, A. Fali, S. T. White, J. R. Matson, S. Liu, N. A. Aghamiri, J. H. Edgar, R. F. Haglund, Y. Abate, J. D. Caldwell, *Nat. Commun.* **2018**, *9*, 4371.
[25] S. Dai, J. Zhang, Q. Ma, S. Kittiwatanakul, A. McLeod, X. Chen, S. G. Corder, K. Watanabe, T. Taniguchi, J. Lu, Q. Dai, P. Jarillo-Herrero, M. Liu, D. N. Basov, *Adv. Mater.* **2019**, *31*, 1900251.
[26] R. Arenal, A. C. Ferrari, S. Reich, L. Wirtz, J. Y. Mevellec, S. Lefrant, A. Rubio, A. Loiseau, *Nano Lett.* **2006**, *6*, 1812.
[27] R. V. Gorbachev, I. Riaz, R. R. Nair, R. Jalil, L. Britnell, B. D. Belle, E. W. Hill, K. S. Novoselov, K. Watanabe, T. Taniguchi, A. K. Geim, P. Blake, *Small* **2011**, *7*, 465.
[28] H.-T. Chen, A. J. Taylor, N. Yu, *Rep. Prog. Phys.* **2016**, *79*, 076401.
[29] S. M. Kim, A. Hsu, M. H. Park, S. H. Chae, S. J. Yun, J. S. Lee, D.-H. Cho, W. Fang, C. Lee, T. Palacios, M. Dresselhaus, K. K. Kim, Y. H. Lee, J. Kong, *Nat. Commun.* **2015**, *6*, 8662.
[30] S. Dai, Q. Ma, Y. Yang, J. Rosenfeld, M. D. Goldflam, A. McLeod, Z. Sun, T. I. Andersen, Z. Fei, M. Liu, Y. Shao, K. Watanabe, T. Taniguchi, M. Thiemens, F. Keilmann, P. Jarillo-Herrero, M. M. Fogler, D. N. Basov, *Nano Lett.* **2017**, *17*, 5285.
[31] N. Ocelic, A. Huber, R. Hillenbrand, *Appl. Phys. Lett.* **2006**, *89*, 101124.
[32] K. K. Kim, A. Hsu, X. Jia, S. M. Kim, Y. Shi, M. Hofmann, D. Nezich, J. F. Rodriguez-Nieva, M. Dresselhaus, T. Palacios, J. Kong, *Nano Lett.* **2012**, *12*, 161.
[33] D. C. Joshua, L. Lindsay, V. Giannini, I. Vurgaftman, L. R. Thomas, A. M. Stefan, J. G. Orest, *Nanophotonics* **2015**, *4*, 44.
[34] A. J. Giles, S. Dai, I. Vurgaftman, T. Hoffman, S. Liu, L. Lindsay, C. T. Ellis, N. Assefa, I. Chatzakis, T. L. Reinecke, J. G. Tischler, M. M. Fogler, J. H. Edgar, D. N. Basov, J. D. Caldwell, *Nat. Mater.* **2017**, *17*, 134.
[35] J. A. Gerber, S. Berweger, B. T. O'Callahan, M. B. Raschke, *Phys. Rev. Lett.* **2014**, *113*, 055502.
[36] D. Alcaraz Iranzo, S. Nanot, E. J. C. Dias, I. Epstein, C. Peng, D. K. Efetov, M. B. Lundeberg, R. Parret, J. Osmond, J.-Y. Hong, J. Kong, D. R. Englund, N. M. R. Peres, F. H. L. Koppens, *Science* **2018**, *360*, 291.
[37] N. Rivera, T. Christensen, P. Narang, *Nano Lett.* **2019**, *19*, 2653.
[38] A. Nemilentsau, T. Low, G. Hanson, *Phys. Rev. Lett.* **2016**, *116*, 066804.
[39] Z. Liu, L. Ma, G. Shi, W. Zhou, Y. Gong, S. Lei, X. Yang, J. Zhang, J. Yu, K. P. Hackenberg, A. Babakhani, J.-C. Idrobo, R. Vajtai, J. Lou, P. M. Ajayan, *Nat. Nanotechnol.* **2013**, *8*, 119.
[40] L. Liu, J. Park, D. A. Siegel, K. F. McCarty, K. W. Clark, W. Deng, L. Basile, J. C. Idrobo, A.-P. Li, G. Gu, *Science* **2014**, *343*, 163.
[41] S. R. Sales de Mello, M. E. H. Maia da Costa, C. M. Menezes, C. D. Boeira, F. L. Freire, F. Alvarez, C. A. Figueroa, *Sci. Rep.* **2017**, *7*, 3242.
[42] S. Kajita, M. Tohyama, H. Washizu, T. Ohmori, H. Watanabe, S. Shikata, *Tribol. Online* **2015**, *10*, 156.
[43] B. Lyu, H. Li, L. Jiang, W. Shan, C. Hu, A. Deng, Z. Ying, L. Wang, Y. Zhang, H. A. Bechtel, M. C. Martin, T. Taniguchi, K. Watanabe, W. Luo, F. Wang, Z. Shi, *Nano Lett.* **2019**, *19*, 1982.
[44] S. Dai, M. Tymchenko, Y. Yang, Q. Ma, M. Pita-Vidal, K. Watanabe, T. Taniguchi, P. Jarillo-Herrero, M. M. Fogler, A. Alù, D. N. Basov, *Adv. Mater.* **2018**, *30*, 1706358.
[45] P. Li, I. Dolado, F. J. Alfaro-Mozaz, A. Y. Nikitin, F. Casanova, L. E. Hueso, S. Vélez, R. Hillenbrand, *Nano Lett.* **2017**, *17*, 228.

ADVANCED MATERIALS

Supporting Information

for *Adv. Mater.*, DOI: 10.1002/adma.201806603

Phonon Polaritons in Monolayers of Hexagonal Boron Nitride

Siyuan Dai, Wenjing Fang, Nicholas Rivera, Yijing Stehle, Bor-Yuan Jiang, Jialiang Shen, Roland Yingjie Tay, Christopher J. Ciccarino, Qiong Ma, Daniel Rodan-Legrain, Pablo Jarillo-Herrero, Edwin Hang Tong Teo, Michael M. Fogler, Prineha Narang, Jing Kong, and Dimitri N. Basov**

Supporting Information

Phonon Polaritons in Monolayers of Hexagonal Boron Nitride

Siyuan Dai, Wenjing Fang, Nicholas Rivera, Yijing Stehle, Bor-Yuan Jiang, Jialiang Shen, Roland Yingjie Tay, Christopher J. Ciccarino, Qiong Ma, Daniel Rodan-Legrain, Pablo Jarillo-Herrero, Edwin Hang Tong Teo, Michael M. Fogler, Prineha Narang, Jing Kong, D. N. Basov**

1. Extraction of the polariton wavelength from the imaging data

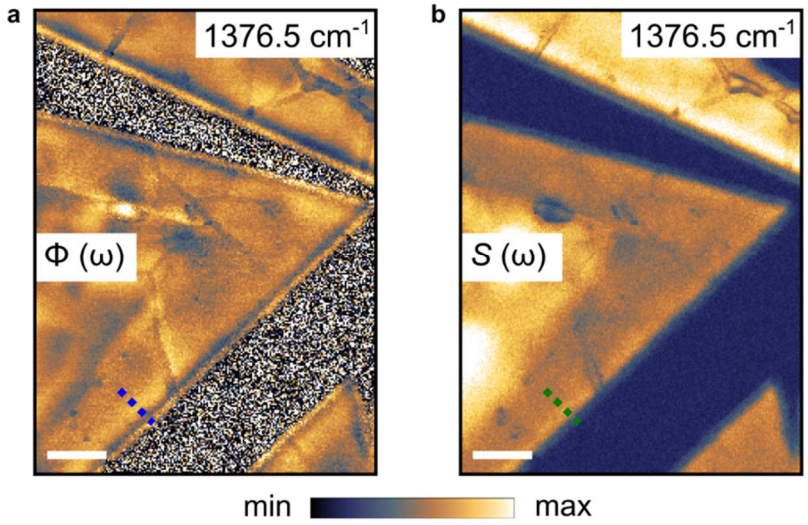

Figure S1. s-SNOM phase (a) and amplitude (b) image of surface phonon polaritons in monolayer hBN at IR frequency $\omega = 1376.5\ \mathrm{cm}^{-1}$. Scale bar: 500 nm.

Representative scattering type scanning near-field optical microscopy (s-SNOM) phase $\Phi(\omega)$ and amplitude $S(\omega)$ images of phonon polaritons in monolayer hBN are shown in **Figure S1**. Our procedure for analyzing polaritonic features in these images starts with selecting suitable line cuts to obtain representative line profiles of Φ and S. Such profiles (taken along the blue and green dotted lines in **Figure S1a-b**) plotted as functions of the distance L from the crystal edge are presented in **Figure S2a-b**. Near the edge, at $0 < L < 200$ nm, both the phase (**Figure S2a**) and the amplitude (**Figure S2b**) reveal signal oscillations or, as we call them, polariton interference fringes. Similar to what has been observed in previous studies,[1, 2] the maxima in Φ occur closer to the edge (at smaller L) compared to those in S. The first maximum of Φ is practically at $L = 0$, while the first

maximum of S is at $L \approx 100\ \mathrm{nm}$. At the latter distance, the polariton wave gets significantly damped. As a result, we resolve two maxima in Φ but only one in S.

The second step in determining the polariton wavelength λ and damping γ is to fit the line profiles to the results of numerical simulations. Our final fit shown in **Figure S2c-d** corresponds to $\lambda = 280\ \mathrm{nm}$ and $\gamma = 0.57$. The details of the fitting procedure are as follows. The simulations are done using a previously developed electromagnetic solver in which hBN is modeled as a two-dimensional (2D) material and the s-SNOM tip is approximated by an elongated conducting spheroid.[3, 4]. The input parameter for the solver is the complex polariton momentum $K = k + ik''$, which determines $\lambda = 2\pi/k$ and the dimensionless damping factor $\gamma = k''/k$. The simulation algorithm first converts k into the sheet conductivity based on the formula[6]

$$K = \frac{i\omega\kappa}{2\pi\sigma_{2D}}, \qquad \text{(S1)}$$

and then solves Maxwell's equation for the charges and currents on the tip and hBN self-consistently. For the purpose of fitting, λ and γ serve as the two adjustable parameters.

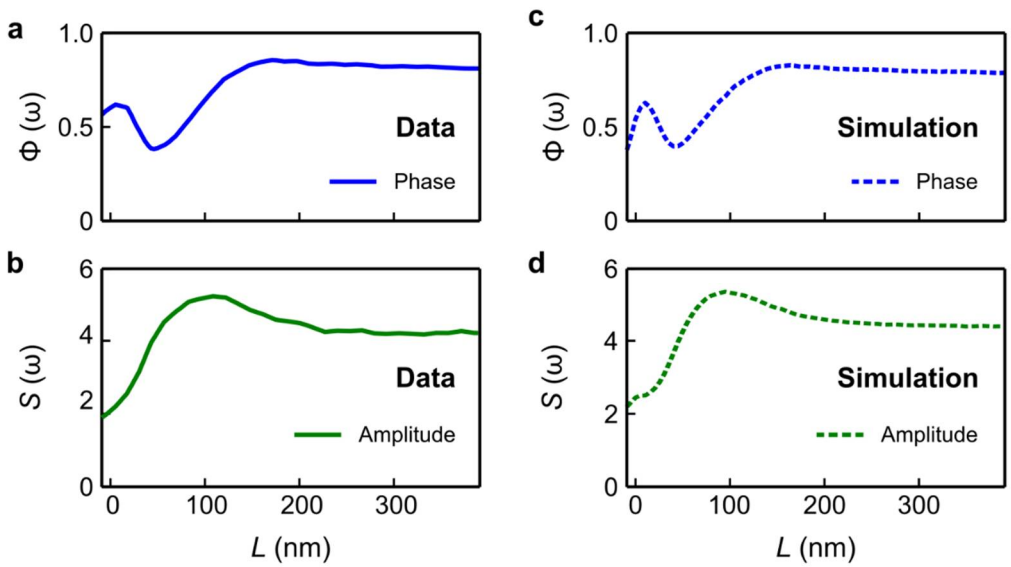

Figure S2. Experimental and simulation results for monolayer hBN. a) and b), Experimental s-SNOM phase (a) and amplitude (b) take along the dashed lines in **Figure S1a,b**. **c**,**d** Simulated s-SNOM phase (c) and amplitude (d). Infrared frequency $\omega = 1376.5\ \mathrm{cm}^{-1}$.

However, the conductivity σ_{2D} that they define through Eq. (S1) can be related to the fundamental response function of hBN – the permittivity tensor ε_1^a – as will be discussed in Section 2. Note that we use the subscript $j = 0, 1, 2$ to label, from top to bottom, the media comprising our system: vacuum, hBN, and SiO_2 substrate, respectively. We also use the superscripts $a = t, z$ for the directions across (along) the z-axis. Finally, parameter κ in Eq. (S1) is the effective permittivity of the environment, which is the average of the permittivities of vacuum ($\varepsilon_0 = 1$) and SiO_2 substrate (ε_2):

$$\kappa = \frac{\varepsilon_0 + \varepsilon_2}{2}. \qquad \text{(S2)}$$

At frequencies of interest, $\omega = 1360\text{–}1400\ \mathrm{cm}^{-1}$, we estimate $\varepsilon_2 = 0.81\text{–}0.96$ per Ref [5].

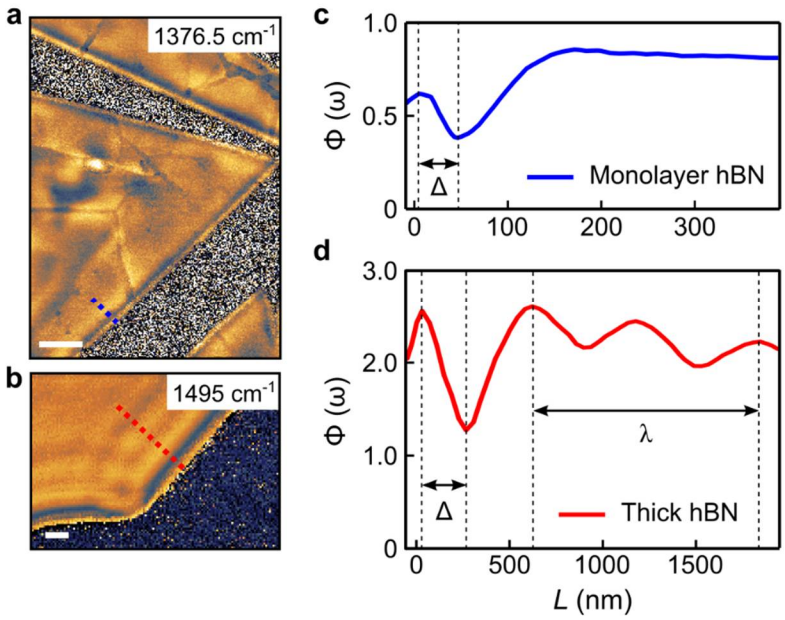

Figure S3. Data from monolayer and thick hBN. a), s-SNOM phase image of monolayer hBN at frequency $\omega = 1376.5\ \mathrm{cm}^{-1}$. b), s-SNOM phase image of thick hBN at IR frequency $\omega = 1495\ \mathrm{cm}^{-1}$. c), s-SNOM line trace taken along blue dotted line in (a). d), s-SNOM line trace taken along red dotted line in (b). Scale bar: 500 nm.

We also employed another method to extract λ, which is less rigorous but is simpler and quicker. This second method is to measure the distance Δ between the positions of the first maxima and minima of the Φ data (**Figure S3**) and then calculate the polariton wavelength as $\lambda = \alpha\Delta$. We determined that the scaling factor is $\alpha = \lambda/\Delta \approx 4.9$ in thicker hBN samples

where many polariton fringes are observed (**Figure S3d**). Assuming the same scaling factor describes monolayer hBN, we find $\lambda = 260\ \mathrm{nm}$ for the data in **Figure S2a**. The difference of the two determinations (via fitting to numerical simulations and via scaling) is about 8%, which is within the uncertainty of the first method.

2. Theoretical models for phonon polaritons in atomically thin hBN

The dispersion relation of phonon polaritons in hBN has been studied in a number of previous works.[6-8] In theory, the polariton dispersion contains multiple branches whose total number inside the Restshrahlen band $\omega_{\mathrm{TO}}^{t} < \omega < \omega_{\mathrm{LO}}^{t}$ of hBN is equal to the number N of atomic layers. Here ω_{TO}^{t} (ω_{LO}^{t}) is the in-plane TO (LO) frequency. In experiment, only the so-called principal branch is typically observed, as is the case here. The theory predicts that for any N (including $N = 1$) the dispersion of this branch at momenta k of interest is linear[9] [same as Eq. (1) of the main text]:

$$\omega = \omega_{\mathrm{TO}}^{t} + v_g k, \qquad \frac{\omega_{\mathrm{TO}}^{t}}{c} \ll k \ll \frac{1}{d}. \tag{S3}$$

Here c is the speed of light, $d = N d_1$, and $d_1 = 0.34\ \mathrm{nm}$ is the hBN interlayer distance. Below we compare formulas for the the group velocity v_g from three theoretical models.

Model 1 (Lattice dynamics of a few-layer hBN with phenomenological Born charges). This approach gives v_g proportional to the number of layers [9]:

$$v_g = N v_1, \qquad v_1 = \frac{u}{\kappa}, \tag{S4}$$

where κ is given by Eq. (S2). Parameter v_1 was introduced in Eq. (1) of the main text. Parameter u of dimension of velocity is[23]

$$u = \frac{\pi}{\Omega} \frac{m_B + m_N}{m_B m_N} \frac{(Z_B^t)^2}{\omega_{\mathrm{TO}}^{t}}. \tag{S5}$$

where $\Omega = \frac{\sqrt{3}}{2}a^2$ is the in-plane area of the hBN unit cell, $a = 0.25\,\text{nm}$ is the in-plane lattice constant, $m_B = 10.8\,\text{au}$ and $m_N = 14.0\,\text{au}$ are the masses of boron and nitrogen ions, and $Z_B^t = -Z_N^t$ are their Born effective charges (see below).

Model 2 (continuum electrodynamics of an hBN slab). This approach yields

$$K = \frac{i}{d}\frac{\sqrt{\varepsilon_j^z}}{\sqrt{\varepsilon_j^t}}\left[\arctan\left(\frac{i\varepsilon_0}{\varepsilon_1}\right) + \arctan\left(\frac{i\varepsilon_2}{\varepsilon_1}\right)\right], \qquad \varepsilon_j \equiv \sqrt{\varepsilon_j^z}\sqrt{\varepsilon_j^t}. \tag{S6}$$

Equation (S4) is a slight generalization of Eq. (1) of Ref.[1] to the case where all the three media involved are uniaxial, with permittivities $\varepsilon_j^a(\omega)$, see also Section 3. Near ω_{TO}^t, where ε_1^t is large, we can expand the right-hand-side of Eq. (S6) in powers of $1/\varepsilon_1^t$,

$$K = -\frac{2\kappa}{\varepsilon_1^t d}\left(1 + \frac{\Delta\varepsilon}{\varepsilon_1^t} + \cdots\right), \qquad \Delta\varepsilon = \frac{1}{3}\frac{\varepsilon_0^2 - \varepsilon_0\varepsilon_2 + \varepsilon_2^2}{\varepsilon_1^z}, \tag{S7}$$

and adopt the conventional Drude-Lorentz model for the response of hBN:

$$\varepsilon_1^a(\omega) = \varepsilon_1^a(\infty) + \varepsilon_1^a(\infty)\frac{(\omega_{\text{LO}}^a)^2 - (\omega_{\text{TO}}^a)^2}{(\omega_{\text{TO}}^a)^2 - \omega^2 - i\omega\Gamma^a}, \qquad a = z, t. \tag{S8}$$

For example, per Ref.[10, 11] of the main text, at room temperature, $\varepsilon_1^t(\infty) = 4.90$, $\omega_{\text{TO}}^t = 1367\,\text{cm}^{-1}$, $\omega_{\text{LO}}^t = 1614\,\text{cm}^{-1}$. Equation (S7) matches Eqs. (S3)-(S4) if we neglect the correction proportional to $\Delta\varepsilon$ in Eq. (S7) and the damping rate Γ^t in Eq. (S8). The matching yields the following formula for the characteristic velocity u:

$$u = \frac{(\omega_{\text{LO}}^t)^2 - (\omega_{\text{TO}}^t)^2}{4\omega_{\text{TO}}^t}\varepsilon_1^t(\infty)d_1. \tag{S9}$$

In turn, Eq. (S9) matches Eq. (S5) if

$$(\omega_{\text{LO}}^t)^2 - (\omega_{\text{TO}}^t)^2 = \frac{4\pi}{\Omega d_1}\frac{m_B + m_N}{m_B m_N}\frac{(Z_B^t)^2}{\varepsilon_1^t(\infty)}, \tag{S10}$$

which is a well known result. For bulk hBN, we infer $u = 4.2 \times 10^6\,\text{cm/s}$ and $Z_B^t = 2.9e$.

Let us discuss the coefficient $\Delta\varepsilon$ in Eq. (S7). At frequencies of interest, $\omega = 1370 - 1390\,\text{cm}^{-1}$, we estimate $\varepsilon_1^z \approx 3.0$; hence, $\Delta\varepsilon \approx 0.1$. On the other hand, $\varepsilon_1^t(\omega)$ is no less than

100 by absolute value in this frequency range. Therefore, the fractional correction $|\Delta\varepsilon/\varepsilon_1^t| \sim 0.1\%$ in Eq. (S5) is well below the experimental uncertainty. Importantly, this correction represents the effect of the z-axis permittivity of hBN, which is therefore negligible. We can now make an argument that the same conclusion applies to monolayer hBN. A monolayer does not have a significant z-axis polarizability, so it is appropriate to choose $\varepsilon_1^z \approx 1$. This yields $|\Delta\varepsilon/\varepsilon_1^t| \sim 0.3\%$, which is still negligible. Thus, in agreement with the Model 1, Eqs. (S3) and (S4) should apply for hBN with any N, including the monolayer. However, as discussed in the main text, ω_{TO}^t in the monolayer and in the bulk may have different values. In fact, prior Raman studies[12, 13] reported a blue shift of ω_{TO}^t by a few wavenumbers in monolayer hBN on SiO_2/Si. As an additional empirical evidence that this may be the case in our experiment, in **Figure S4** we present data obtained from another monolayer hBN sample. The two dashed lines in **Figure S4b** are linear fits to the extracted polariton dispersion, one using the bulk value and the other using a larger value $\omega_{\mathrm{TO}}^t = 1370.5\ \mathrm{cm}^{-1}$ of the TO frequency. The latter gives a better fit, as for the sample discussed in the main text (**Figure 3b**). Although material imperfections and mechanical strain may affect phonon properties of hBN in the experiments,[14] our calculations presented at the end of this Section indicate that the blue shift of ω_{TO}^t may be an intrinsic phenomenon.

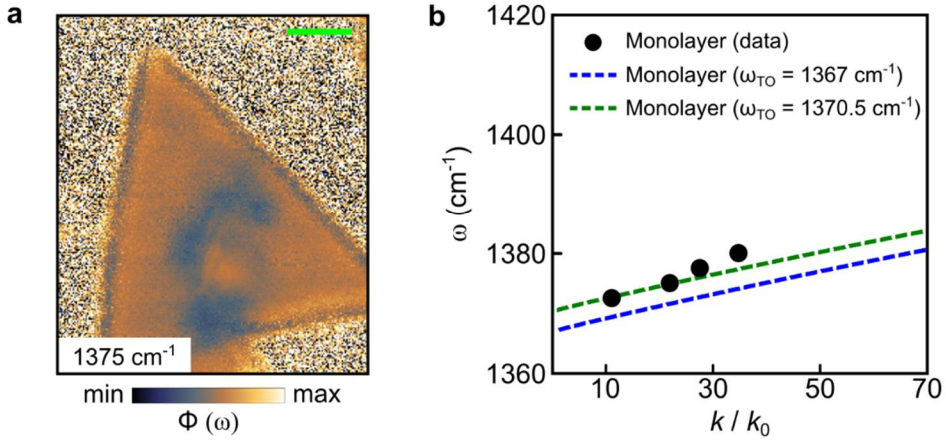

Figure S4. s-SNOM data for the second monolayer hBN sample. a), s-SNOM phase images at frequency $\omega = 1375\ \mathrm{cm}^{-1}$. Scale bar: 500 nm. b), Polariton dispersion. Experimental

data extracted from the images are shown by the dots. Theoretical predictions are indicated with the blue ($\omega_{\mathrm{TO}}^{t} = 1367\ \mathrm{cm}^{-1}$) and green ($\omega_{\mathrm{TO}}^{t} = 1370.5\ \mathrm{cm}^{-1}$) dashed curves.

Model 3 (continuum electrodynamics of a two-dimensional sheet). Another continuum-medium approach[13] already mentioned in Section 1 further approximates the hBN slab by a two-dimensional (2D) material of sheet conductivity $\sigma_{2\mathrm{D}}$. Hence, not only the z-axis response of hBN but also its geometric thickness is ignored. A 2D sheet is known to support a longitudinal collective mode with the dispersion given by Eq. (S1). To compare it with Eq. (S5), we need a model for $\sigma_{2\mathrm{D}}$. The common choice is $\sigma_{2\mathrm{D}} = \sigma^{t} d$, where σ^{t} is the in-plane bulk conductivity. The latter is linked to the in-plane permittivity ε_1^{t} via $\varepsilon_1^{t}(\omega) = 1 + \frac{4\pi i}{\omega}\sigma^{t}(\omega)$. Using these relations, it is straightforward to show that Eqs. (S1) and (S7) agree to the leading order in ε_1^{t} but differ in the magnitude of the correction: Eq. (S7) gives $\Delta\varepsilon = 1$. This difference between the finite-thickness-slab and the 2D-film approximations is still well within the experimental uncertainty. In other words, all the three Models are in agreement.

First-principles calculations. To compute the microscopic parameters in the above formulas, we studied monolayer and bilayer hBN using the density functional perturbation theory (DFPT) within QUANTUM ESPRESSO[15, 16]. We evaluated electronic properties on a $24 \times 24 \times 1$ k-point mesh and phonon properties on a $6 \times 6 \times 1$ q-point mesh. To handle Coulomb interactions we followed Sohier et al.[17] We used the plane-wave basis set with the 30-Hartree energy cutoff and we truncated the Coulomb interaction[18] to remove periodic image effects. The examined three choices of the exchange-correlation potentials: the Perdew-Burke-Ernzerhof (PBE)[19], the solid-state-adapted PBE (PBEsol)[20], and the local-density approximation (LDA).[21] For the bilayer we also took into account van der Waals interactions beyond the PBEsol. For simplicity, we neglected excitonic or substrate-coupling effects. The parameters we extracted for a fully relaxed monolayer system using the PBEsol functional were $Z_B^{t} = -Z_N^{t} = 2.7e$ and $\omega_{\mathrm{TO}}^{t} = 1362.4\ \mathrm{cm}^{-1}$. For the bilayer, we obtained

the same Born charges but lower $\omega_{\mathrm{TO}}^{t} = 1360.4\ \mathrm{cm}^{-1}$. We found that the TO frequency depends on the choice of the exchange-correlation functional. Nevertheless, our calculations support the hypothesis that ω_{TO}^{t} is intrinsically blue shifted, by a few wavenumbers, in the monolayer compared to the bulk hBN, in agreement with our s-SNOM experiments and the prior Raman studies.[17,18]

3. Electric field distribution of phonon polariton eigenmodes in atomically thin hBN

To calculate the field distribution of polariton eigenmodes we use the continuum electrodynamics approach (Model 2) introduced in Section 2. We choose the x-axis in the direction of the polariton momentum K. The two nonzero components of the electric field are $E^{a}(x,z) = e^{a}(z)e^{iKx}$ where $a = x, z$. The amplitudes $e^{a}(z)$ in each of the regions $j = 0,1,2$ (vacuum, hBN, and SiO_2, respectively) are given by

$$\begin{aligned} e^{x}(z) &= A_j e^{-ik_j^z z} + B_j e^{ik_j^z z}\,, \\ e^{z}(z) &= \frac{\varepsilon_j^t}{\varepsilon_j^z}\frac{k}{k_j^z}\left(A_j e^{-ik_j^z z} - B_j e^{ik_j^z z}\right) \end{aligned} \tag{S11}$$

with $A_0 = B_2 = 0$. The quantities k_j^z are the z-axis momenta,

$$k_j^z = \sqrt{\varepsilon_j^t}\sqrt{k_0^2 - \frac{K^2}{\varepsilon_j^z}}\,, \quad \Im\mathrm{m}\, k_j^z > 0\,, \tag{S12}$$

where $k_0 = \omega/c$. For the case of monolayer hBN, we have $B_0 \approx A_2$. Additionally, for highly confined polaritons, $k \gg k_0$, we get

$$e^{x}(z) = e^{x}(0)\exp\left(ik_z^j|z|\right), \qquad e^{z}(z) = \pm i\ \mathrm{sign}(z)\, e^{x}(z)\,. \tag{S13}$$

The z-axis momentum $k_j^z \simeq ik$ is almost entirely imaginary, so that the electric field decays exponentially away from hBN. In **Figure S5** we plot the polariton field distribution along the z-direction at a representative frequency $\omega = 1376.5\ \mathrm{cm}^{-1}$. Note that the x- and z-components of the field have the same absolute value, although the z- component has opposite signs above and below the hBN. By convention, the z-axis confinement length is

defined from the criterion that this absolute value decays by the factor of $e = \exp(1)$. Therefore, polariton confinement length in the z-direction is $2/k = \lambda/\pi$. Following another convention[22], the mode area in the 2D plane is taken to be λ^2. The mode volume of phonon polaritons in monolayer hBN is therefore λ^3/π.

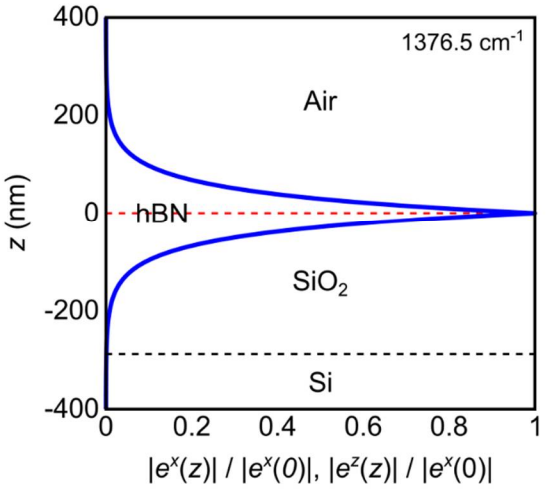

Figure S5. Amplitude of the electric field of a phonon polariton in monolayer hBN at IR frequency $\omega = 1376.5\ \mathrm{cm}^{-1}$.

Finally, for completeness, we list the coefficients A_j and B_j for an arbitrary d:

$$\begin{aligned} A_0 &= 0, & B_0 &= 1 - r_{12}e^{2ik_1^z d}, \\ A_1 &= 1, & B_1 &= -r_{12}e^{2ik_1^z d}, \\ A_2 &= (1 - r_{12})e^{i(k_1^z - k_2^z)d}, & B_2 &= 0\,. \end{aligned} \tag{S14}$$

Here r_{ij} are the Fresnel reflection coefficients for a i-j interface:

$$r_{ij} = \frac{Q_j - Q_i}{Q_j + Q_i}\,, \qquad Q_j = \frac{\varepsilon_j^t}{k_j^z}\,. \tag{S15}$$

Note also that the eigenmode equation leading to Eq. (S6) is[1]

$$1 + r_{01}r_{12}e^{2ik_1^z d} = 0\,. \tag{S16}$$

It correspond to the poles of the reflection coefficient $r_p(K, \omega)$ of a P-polarized wave incident on the sample[1]:

$$r_p = \frac{r_{01} + r_{12}e^{2ik_1^z d}}{1 + r_{01}r_{12}e^{2ik_1^z d}}. \quad \text{(S17)}$$

References

[1] J. A. Gerber, S. Berweger, B. T. O'Callahan, M. B. Raschke, *Physical Review Letters* **2014**, *113*, 055502.
[2] Z. Shi, H. A. Bechtel, S. Berweger, Y. Sun, B. Zeng, C. Jin, H. Chang, M. C. Martin, M. B. Raschke, F. Wang, *ACS Photonics* **2015**, *2*, 790.
[3] Z. Fei, A. S. Rodin, G. O. Andreev, W. Bao, A. S. McLeod, M. Wagner, L. M. Zhang, Z. Zhao, M. Thiemens, G. Dominguez, M. M. Fogler, A. H. C. Neto, C. N. Lau, F. Keilmann, D. N. Basov, *Nature* **2012**, *487*, 82.
[4] G. X. Ni, H. Wang, J. S. Wu, Z. Fei, M. D. Goldflam, F. Keilmann, B. Özyilmaz, A. H. Castro Neto, X. M. Xie, M. M. Fogler, D. N. Basov, *Nature Materials* **2015**, *14*, 1217.
[5] A. Kučírková, K. Navrátil, *Applied Spectroscopy* **1994**, *48*, 113.
[6] A. Kumar, T. Low, K. H. Fung, P. Avouris, N. X. Fang, *Nano Letters* **2015**.
[7] S. Dai, Z. Fei, Q. Ma, A. S. Rodin, M. Wagner, A. S. McLeod, M. K. Liu, W. Gannett, W. Regan, K. Watanabe, T. Taniguchi, M. Thiemens, G. Dominguez, A. H. C. Neto, A. Zettl, F. Keilmann, P. Jarillo-Herrero, M. M. Fogler, D. N. Basov, *Science* **2014**, *343*, 1125.
[8] K. H. Michel, B. Verberck, *Physical Review B* **2011**, *83*, 115328.
[9] N. Rivera, T. Christensen, P. Narang, *Nano Letters* **2019**.
[10] J. D. Caldwell, A. V. Kretinin, Y. Chen, V. Giannini, M. M. Fogler, Y. Francescato, C. T. Ellis, J. G. Tischler, C. R. Woods, A. J. Giles, M. Hong, K. Watanabe, T. Taniguchi, S. A. Maier, K. S. Novoselov, *Nature Communications* **2014**, *5*, 5221.
[11] G. X. Ni, A. S. McLeod, Z. Sun, L. Wang, L. Xiong, K. W. Post, S. S. Sunku, B. Y. Jiang, J. Hone, C. R. Dean, M. M. Fogler, D. N. Basov, *Nature* **2018**, *557*, 530.
[12] Q. Cai, D. Scullion, A. Falin, K. Watanabe, T. Taniguchi, Y. Chen, E. J. G. Santos, L. H. Li, *Nanoscale* **2017**, *9*, 3059.
[13] R. V. Gorbachev, I. Riaz, R. R. Nair, R. Jalil, L. Britnell, B. D. Belle, E. W. Hill, K. S. Novoselov, K. Watanabe, T. Taniguchi, A. K. Geim, P. Blake, *Small* **2011**, *7*, 465.
[14] L. H. Li, Y. Chen, *Advanced Functional Materials* **2016**, *26*, 2594.
[15] P. Giannozzi, S. Baroni, N. Bonini, M. Calandra, R. Car, C. Cavazzoni, D. Ceresoli, G. L. Chiarotti, M. Cococcioni, I. Dabo, A. Dal Corso, S. de Gironcoli, S. Fabris, G. Fratesi, R. Gebauer, U. Gerstmann, C. Gougoussis, A. Kokalj, M. Lazzeri, L. Martin-Samos, N. Marzari, F. Mauri, R. Mazzarello, S. Paolini, A. Pasquarello, L. Paulatto, C. Sbraccia, S. Scandolo, G. Sclauzero, A. P. Seitsonen, A. Smogunov, P. Umari, R. M. Wentzcovitch, *Journal of Physics: Condensed Matter* **2009**, *21*, 395502.
[16] S. Grimme, *Journal of Computational Chemistry* **2006**, *27*, 1787.
[17] T. Sohier, M. Gibertini, M. Calandra, F. Mauri, N. Marzari, *Nano Letters* **2017**, *17*, 3758.
[18] T. Sohier, M. Calandra, F. Mauri, *Physical Review B* **2017**, *96*, 075448.
[19] J. P. Perdew, K. Burke, M. Ernzerhof, *Physical Review Letters* **1996**, *77*, 3865.
[20] J. P. Perdew, A. Ruzsinszky, G. I. Csonka, O. A. Vydrov, G. E. Scuseria, L. A. Constantin, X. Zhou, K. Burke, *Physical Review Letters* **2008**, *100*, 136406.
[21] J. P. Perdew, A. Zunger, *Physical Review B* **1981**, *23*, 5048.
[22] D. Alcaraz Iranzo, S. Nanot, E. J. C. Dias, I. Epstein, C. Peng, D. K. Efetov, M. B. Lundeberg, R. Parret, J. Osmond, J.-Y. Hong, J. Kong, D. R. Englund, N. M. R. Peres, F. H. L. Koppens, *Science* **2018**, *360*, 291.